Article

Electron Spin Density on the N-Donor Atoms of Cu(II)−(Bis)oxamidato Complexes As Probed by a Pulse ELDOR Detected NMR

Azar Aliabadi,[†] Ruslan Zaripov,[‡] Kev Salikhov,[‡] Violeta Voronkova,[‡] Evgeniya Vavilova,[‡] Mohammad A. Abdulmalic,[§] Tobias Rüffer,[§] Bernd Büchner,[†,∥] and Vladislav Kataev*,[†,‡]

[†]Leibniz Institute for Solid State and Materials Research IFW Dresden, D-01171 Dresden, Germany
[‡]Zavoisky Physical Technical Institute, Russian Academy of Sciences, 420029 Kazan, Russia
[§]Technische Universität Chemnitz, Fakultät für Naturwissenschaften, Strasse der Nationen 62, D-09111 Chemnitz, Germany
[∥]Institut für Festkörperphysik, Technische Universität Dresden, D-01062 Dresden, Germany

ABSTRACT: We have applied the pulse ELDOR detected NMR (EDNMR) technique to determine the tensors of the transferred Cu $(S = 1/2) - {}^{14}$N $(I = 1)$ hyperfine (HF) interaction in single crystals of diamagnetically diluted mononuclear o-phenylenebis(N(R)-oxamide) complexes of $[{}^{n}Bu_4N]_2[Cu(opboR_2)]$ (R = Et **1**, ^{n}Pr **2**) (1%) in a host lattice of $[{}^{n}Bu_4N]_2[Ni(opboR_2)]$ (R = Et **3**, ^{n}Pr **4**) (99%) (**1@3** and **2@4**)). To facilitate the analysis of our EDNMR data and to analyze possible manifestations of the nuclear quadrupole interaction in the EDNMR spectra, we have treated a model electron−nuclear system of the coupled $S = 1/2$ and $I = 1$ spins using the spin density matrix formalism. It appears that this interaction yields a peculiar asymmetry of the EDMR spectra that manifests not only in the shift of the positions of the EDNMR lines that correspond to the forbidden EPR transitions, as expected, but also in the intensities of the EDNMR lines. The symmetric shape of the experimental spectra suggests the conclusion that, in the studied complexes, the quadrupole interaction is negligible. This has simplified the analysis of the spectra. The HF tensors of all four N donor atoms could be accurately determined. On the basis of the HF tensors, an estimate of the spin density transferred from the central paramagnetic Cu(II) ion to the N donor atoms reveals its unequal distribution. We discuss possible implications of our estimates for the magnetic exchange paths and interaction strengths in respective trinuclear complexes $[Cu_3(opboR_2)(pmdta)_2](NO_3)_2$ (R = Et **6**, ^{n}Pr **7**).
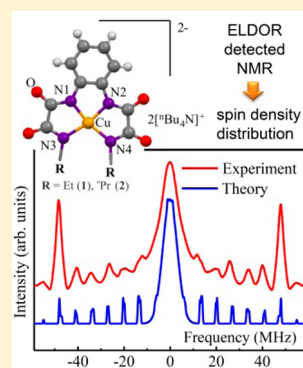
1. INTRODUCTION

Several pulse techniques, such as electron spin echo envelope modulation (ESEEM),[1] discrete saturation (DS),[2−4] Fourier transform (FT)-ESR detected NMR,[5] pulse ENDOR,[6,7] and pulse ELDOR detected NMR (EDNMR),[5,8] are used to measure the hyperfine (HF) interaction in disordered systems. Information about the HF constants can be used to estimate the spin density on both the magnetic ion center and also on surrounding atoms. In measuring small HF interactions, the EDNMR method often appears to be more sensitive than the other techniques mentioned. It becomes particularly advantageous at high magnetic fields corresponding to the Q- and W-band frequencies, as has been shown by several groups (see, e.g., refs 9−14). The EDNMR measurement protocol contains a selective microwave (mw) pulse of frequency $\omega_{mw}^{(1)}$, which should excite a forbidden electron−nuclear level transition $(\Delta m_s = \pm 1$ and $\Delta m_I = \pm 1)$ and burn "holes" in an ESR line (here, we use terminology from ref 5). The integration of the free induction decay (FID) after an application of a mw pulse of frequency $\omega_{mw}^{(2)}$ is recorded as the pattern of holes that represents the EDNMR spectrum. Evaluation of the spectra can yield a reliable determination of the transferred HF tensors and can thus provide an important input for the analysis of the

electron spin distribution, e.g., on the ligands of a transition metal (TM) ion in metal organic molecules. In turn, knowledge of the spin density distribution facilitates the assessment of magnetic exchange pathways in multinuclear TM molecular complexes and helps in understanding their magnetic properties.

One of the interesting classes of magnetically active molecular materials is transition metal−(bis)oxamidato complexes. They can be utilized as suitable building blocks for the synthesis of respective polymetallic TM (bis)oxamidato complexes that are considered possible candidates for use in molecular electronic devices. Understanding of exchange pathways in such complexes is therefore important for a rational design of new materials with improved intramolecular magnetic interactions between the metal ions.

It has been shown that the spin density distribution for Cu(II)-containing (bis)oxamidato-type mononuclear com-

plexes can be an indicator of the strength of the magnetic superexchange interaction J in corresponding trinuclear complexes[15] and thus provide a clue to the control of the magnetic exchange interaction in their corresponding trinuclear complexes. In our recent work,[10] we have studied magnetic properties of several new trinuclear complexes, including $[Cu_3(opboR_2)(pmdta)_2](NO_3)_2$ (R = Me **5**, Et **6**, ^{n}Pr **7**). To assess magnetic exchange interactions, we studied the HF tensors for Cu(II) ion and N donor atoms of respective diamagnetically diluted single crystalline mononuclear complexes of $[^nBu_4N]_2[Cu(opboR_2)]$ (R = Et **1**, ^{n}Pr **2**) (1%) in the host lattice of $[^nBu_4N]_2[Ni(opboR_2)]$ (R = Et **3**, ^{n}Pr **4**) (99%) (**1@3** and **2@4**), respectively, by cw ESR and ENDOR experiments at 10 GHz.[16] On the basis of the obtained ESR parameters, the spin density distribution of the anionic complex fragments of **1** and **2** were calculated using theoretical models.[17,18] In particular, using the pulse Davies ENDOR technique, we were able to obtain the HF tensor of the individual N donor atom in **1** by measuring a single crystal of **1@3** at 10 GHz, which is not possible by a cw ESR experiment. Consequently, we could obtain insights into magnetic superexchange paths in corresponding trinuclear complex **6**. Unfortunately, the accuracy of the determination of the HF tensors was limited due to a low signal-to-noise (S/N) ratio and the overlap of the lines arising from ^{14}N and protons (^{1}H) in some orientations. Possible reasons for a low S/N ratio could be long duration of pulse sequence used in pulse Davies ENDOR technique and temperature instabilities due to sample heating by the radio frequency pulse. Therefore, this technique requires a large number of scans to obtain an ENDOR spectrum, and it is time consuming. In this respect, the EDNMR technique could be advantageous because it has a shorter duration of pulse sequence. Further improvement can be achieved by performing the EDNMR experiments at a higher frequency to avoid possible covering of a signal by the so-called central hole and removing the overlap of the lines from ^{14}N and protons (^{1}H).

In the present work, EDNMR experiments have been carried out to verify and refine the HF tensor for the individual N donor atoms of **1** and to accurately determine the HF tensor for the individual N donor atoms of **2**. Furthermore, with the aid of a standard model that relates the HF constants to the spin densities, we estimated a transfer of the spin density from Cu(II) to the nitrogen donor atoms in **1** and **2** using the HF tensors as input parameters. Finally, we discussed the relevance of these estimates for the superexchange paths and magnetic interaction strength in respective trinuclear complexes **6** and **7**. On the theoretical side, we treat a model system of an electron spin $S = 1/2$ coupled to a nuclear spin $I = 1$ using the spin density matrix formalism. A model of coupled spins $S = 1/2$ and $I > 1/2$ has been discussed already in several works[9−14] and, very recently, a general scheme of a theoretical description of the EDNMR spectra using the spin density matrix has also been proposed.[12] Here, we elaborate this approach in more detail to facilitate the analysis of our experimental data. Furthermore, we consider the effect of the nuclear quadrupole interaction on the EDNMR spectrum. The problem of the quadrupole interaction has been addressed before in the basic theoretical treatment of the DS,[2−4] the FT-ESR detected NMR,[5] and the EDNMR,[5,8,10,13,14] though only shifts of the spin energy levels induced by the quadrupole interaction have been considered. However, the quadrupole interaction can also change the transition matrix elements induced by the mw

pulses in the course of the EDNMR experiment. Note that the nuclear quadrupole interaction can essentially affect the ESEEM data (see, e.g., ref 19). Indeed, we have found that including a sizable quadrupole interaction in the model yields asymmetry not only in the positions but also in the intensities of the lines in the EDNMR spectrum.

2. EDNMR TREATMENT FOR $S = 1/2$ AND $I = 1$ MODEL ELECTRON−NUCLEAR SYSTEM

Compared to a relatively simple case of the model $S = 1/2$ and $I = 1/2$ system, which has been comprehensively studied in several works (see, e.g., refs 5 and 8), the case of the Cu(II) spin $S = 1/2$ coupled to the ^{14}N nuclear spins $I = 1$ in the complexes studied in the present work is more complicated due to a larger nuclear spin multiplicity and the possible presence of an additional nuclear quadrupole interaction generally expected for nuclei with $I > 1/2$.

The relevant spin Hamiltonian (in angular frequency rad/s units) reads

$$\mathcal{H} = \left(\frac{\mu_B}{\hbar}\right)\vec{S}\mathbf{g}\vec{B}_0 - \gamma_n B_0 I_z + \vec{S}\mathbf{A}\vec{I} + \vec{I}\mathbf{D}\vec{I} \tag{1}$$

It contains the Zeeman interaction of electron and nuclear spins with an external magnetic field, the HF interaction, and the quadrupole interaction terms. μ_B and γ_n are the Bohr magneton and nuclear gyromagnetic ratio, respectively. Recently, a general scheme of a theoretical description of the EDNMR spectra using the spin density matrix has been described in ref 12. Below, we elaborate on this approach in more detail and also elucidate whether the nuclear quadrupole interaction can give a peculiar manifestation. To simplify the treatment, we assume that the **g**-tensor, the HF interaction tensor (**A**), and the quadrupole interaction tensor (**D**) have collinear principal axes X,Y,Z. In addition, we suppose that these tensors obey an axial symmetry. In this case, the anisotropic parts of **A** (and **D**) tensors have the property $A_{XX} = A_{YY} = -(1/2)A_{ZZ}$. The direction of the external magnetic field B_0 in the molecular X,Y,Z frame is characterized by a polar angle (θ) and an azimuthal angle (φ). We chose the magnetic field direction as the z-axis of the laboratory frame. Under these conditions and keeping only secular with respect to S_z terms, eq 1 transforms into the spin Hamiltonian

$$\mathcal{H} = \omega_S S_Z - \omega_I I_Z + T_{ZZ} S_Z I_Z + T_{ZX} S_Z I_X + D_{ZZ} I_Z^2 \tag{2}$$

Here,

$$T_{ZZ} = (A_{ZZ} + 2A_{XX})/3 - (1/3)(A_{ZZ} - A_{XX})(1 - 3\cos^2\theta)$$

$$T_{ZX} = (1/2)(A_{ZZ} - A_{XX})\sin 2\theta$$

$$D_{ZZ} = (-1/3)D(1 - 3\cos^2\theta)$$

$$\omega_s = (\mu_B/\hbar)g_{eff}B_0$$

$$g_{eff} = g_{ZZ}^2\cos^2\theta + g_{XX}^2\sin^2\theta$$

$$\omega_I = \gamma_n B_0$$

Figure 1 shows an example of the energy levels for the strong HF coupling case ($A > 2\omega_I$). Solid arrows indicate the three allowed ESR transitions, $\Delta m_S = \pm 1$ and $\Delta m_I = 0$. Dashed arrows correspond to forbidden transitions with $\Delta m_S = \pm 1$,
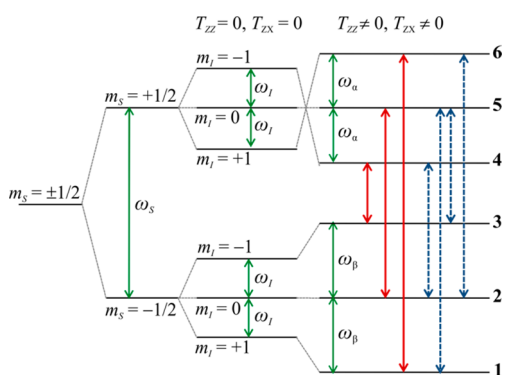
Figure 1. Energy levels diagram of an $S = 1/2$ and $I = 1$ electron–nuclear system. Solid arrows correspond to the three allowed ESR transitions with $\Delta m_S = \pm 1$ and $\Delta m_I = 0$. Dashed arrows correspond to forbidden transitions with $\Delta m_S = \pm 1$ and $\Delta m_I = \pm 1$.

$\Delta m_I = \pm 1$. They arise due to anisotropic (nonsecular) part $T_{ZX}S_Z I_X$ of the HF interaction (eq 2).

When the quadrupole interaction is negligible, there are analytical expressions for these allowed ω_a and forbidden transitions ω_f frequencies.

$$\omega_a = \omega_S; \; \omega_S \pm (\omega_\alpha + \omega_\beta)$$

$$\omega_f = \omega_S \pm \omega_\alpha; \; \omega_S \pm \omega_\beta \qquad (3)$$

where

$$\omega_\alpha = (1/2)\sqrt{(T_{ZX}^2 + (T_{ZZ} - 2\omega_I)^2)},$$

$$\omega_\beta = (1/2)\sqrt{(T_{ZX}^2 + (T_{ZZ} + 2\omega_I)^2)}$$

In principle, there are also forbidden transitions when the nuclear spin projection changes by $\Delta m_I = \pm 2$, but their probability are expected to be much smaller than for the forbidden $\Delta m_S = \pm 1$, $\Delta m_I = \pm 1$ transitions with resonance frequencies $\omega_S \pm (\omega_\alpha + \omega_\beta)$.

A pulse sequence used in our EDNMR experiment is shown in Figure 2. It consists of two mw pulses: a selective preparation
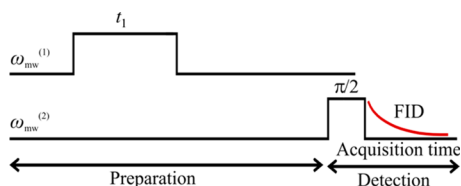

Figure 2. An EDNMR experiment pulse sequence (details in the text).

pulse of frequency $\omega^{(1)}$ and a probe pulse of frequency $\omega^{(2)}$. The excitation of the electron spin system by the selective mw pulse of length $t_{mw}^{(1)}$ burns "holes" in the ESR spectrum, as described in the terminology in ref 5. Depending on the frequency $\omega^{(1)}$, these holes will appear either at allowed or forbidden lines of the ESR spectrum. The probe pulse creates a free induction decay (FID) signal, which is an observable quantity (in short, observable). Its magnitude reflects the presence of holes induced in the preparation period. One can use, as the observable, the FID intensity at a fixed acquisition time after the detection pulse, whereas in experiments, one integrates the FID signal. In the numerical simulations presented below in this section, we use the initial intensity of the FID signal as observable.

In the EDNMR method, a behavior of the observable is influenced by two factors. In principle, the preparation (first) pulse changes populations of spin states and creates spin coherence. However, the time interval between the two pulses in the ENDMR protocol is longer than the spin decoherence time. Therefore, the observable can reflect the population changes induced by the preparation pulse but not the spin coherence created by that pulse. Let us suppose that the preparation pulse has equalized populations of two selected spin states labeled as n and k. Then, transitions between these two states with equal populations induced by the second pulse will not induce the FID signal. Thus, the free induction signal observed in EDNMR experiment as a function of the preparation pulse frequency $\omega^{(1)}$ will exhibit a "hole" as soon as the preparation pulse frequency matches the ESR transition frequency between the n and k states under consideration, i.e., when $\omega^{(2)} = \omega(n \leftrightarrow k)$.

To illustrate the features of the EDNMR observable, we present representative simulated spectra (Figure 3). There, a
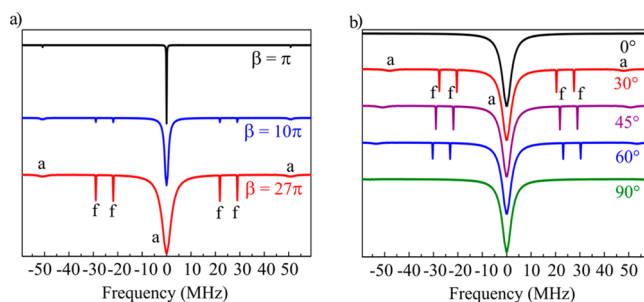

Figure 3. Dependence of the model EDNMR spectrum on the flip angle of the magnetization β caused by the first pulse (a) and on the orientation of the sample in the external magnetic field (b). Common parameters used in both plots are $g_{ZZ} = 2.144$, $g_{XX} = g_{YY} = 2.016$,[16] $A_{ZZ} = 56$ MHz, $A_{XX} = A_{YY} = 45$ MHz, $B_0 = 1.1666$ T, $B_{1d} = 0.22$ G, $t_d = 0.4$ μs, $t_p = 6$ μs. Parameters for (a): $\theta = \pi/4$, $B_{1p} = 0.028$ G (top), $B_{1p} = 0.28$ G (middle), $B_{1p} = 0.8$ G (bottom). Parameters for (b): $\theta = \{0, \pi/6, \pi/4, \pi/3, \pi/2\}$, $B_{1p} = 0.8$ G. These parameters were taken close to the experimentally determined values for the studied complexes (see below). The peaks at approximately ± 51 and 0 MHz correspond to the allowed transitions (a). The peaks at approximately ± 29 and ± 22 MHz correspond to the forbidden transitions (f).

dependence of an average value of the S_y spin component on the preparation pulse frequency calculated at the zero acquisition time (immediately after the probe pulse is switched off) is shown. The algorithm of our simulations is as follows: At time $t = 0$, the spin density operator ρ has the thermal equilibrium value so that one can approximate it as $\rho = -S_z$.[20] In the interval t_1, when the preparation pulse is applied, the spin system develops with the spin Hamiltonian

$$\mathcal{H}_p = \mathcal{H} - \omega^{(1)} S_Z + \omega_{1p} S_X \qquad (4)$$

Here $\mathcal{H}$ is the Hamiltonian of the free dynamics of the spin system given by eq 2. $\omega_{1p} = \gamma_e B_{1p}$ is the electron spin Rabi frequency in the microwave (mw) field of the preparation pulse. To perform a frequency selective excitation, one uses a relatively small magnetic field strength B_{1p}. Thus, at the end of the preparation period, at $t = t_1$, the density matrix equals $\rho(t_1) = -e^{-i\hat{H}_p t_1} S_Z e^{i\hat{H}_p t_1}$. Note that no spin relaxation is included here. To include the spin relaxation, one has to solve a proper kinetic equation for the spin density matrix. Further, we suppose that the interval between the preparation and probe pulses is longer

than the spin decoherence time (T_2) but shorter than the spin–lattice relaxation time (T_1). Thus, in the basis of the eigenstates of the spin-Hamiltonian $\mathcal{H}$ (eq 2), the representation of all off-diagonal elements of $\rho(t_1)$ become zero. Therefore, the detection (probe) pulse is applied to the system in the state described by the spin density matrix, which consists only of the diagonal elements of $\rho(t_1)$. Let us denote it as $\rho_{\text{diag}}(t_1)$. During the action of the probe (detection) pulse, the spin dynamics develops with the spin Hamiltonian

$$\mathcal{H}_d = \mathcal{H} - \omega^{(2)} S_Z + \omega_{1d} S_X \tag{5}$$

where $\omega_{1d} = \gamma_e B_{1d}$.

At the end of the probe pulse, the spin density matrix equals $\rho(t_2) = -e^{-iH_d t_2} \rho_{\text{diag}}(t_1) e^{iH_d t_2}$. Then, we calculate the average value of S_Y as

$$\langle S_Y \rangle = \text{Tr}(\rho(t_2) S_Y) \tag{6}$$

Here, $\rho(t_2)$ means the spin density operator at the moment when the probe mw pulse is switched off. Note that the observed EDNMR signal is proportional to the calculated $<S_Y>$.

Figure 3 shows the lines that manifest a saturation effect for three allowed and four forbidden transitions, as expected (see Figure 1). Positions of the lines are fully determined by the free dynamics as set by spin Hamiltonian (eq 2). The amplitude of the lines is governed by two factors. First, it depends on the offsets of the line positions from the observation pulse frequency $\Delta = \omega^{(2)} - \omega_{nk}$ (ω_{nk} denotes the resonance transition frequency n↔k). Contribution of any ESR transitions to the observable in the EDNMR experiment depends on their frequency offset Δ according to the well-known expression

$$P_{\text{offset}} = \left(\frac{\omega_{1d}^2}{\Delta^2 + \omega_{1d}^2} \right) \sin^2 \left(\frac{(\Delta^2 + \omega_{1d}^2)^{1/2} t_d}{2} \right) \tag{7}$$

Here, t_d is the duration of the detection pulse. When the offset is larger than the Rabi frequency of the detection pulse, then the amplitude of the corresponding line should decrease as ω_{1d}^2 / Δ^2. In the simulations presented for the central component of the ESR spectrum, the offset is $\Delta = 0$, which corresponds to the zero value of the nuclear spin projection. This explains why, in the EDNMR spectra shown in Figure 3, the central line is deep, whereas the two side lines, which also correspond to the allowed ESR transitions, are shallow. Second, the amplitude of the lines in the EDNMR spectrum depends on the Rabi frequency and on the duration of the preparation pulse. We suppose that the preparation pulse field is weak so that it performs frequency selective excitation, i.e., excites transitions between two definite states of the spin system. These two states involved into the transition can be considered as an effective two-level system that can be described by the gyroscopic model.[21] For the allowed ESR transitions, the Rabi frequency for the preparation pulse field equals ω_{1p} (eq 4). For the forbidden ESR transitions with $\Delta m_S = \pm 1$ and $\Delta m_I = \pm 1$, the effective Rabi frequencies are

$$\omega_{1p,f1} = (\omega_{1p}/\sqrt{2}) T_{ZX}/\omega_\alpha \ll \omega_{1p}$$

$$\omega_{1p,f2} = (\omega_{1p}/\sqrt{2}) T_{ZX}/\omega_\beta \ll \omega_{1p} \tag{8}$$

The amplitude of a line that corresponds to a given resonance transition is determined by the rotation angle ξ,

which equals to the product of the corresponding Rabi frequency and the pulse duration

$$\xi_{\text{allowed}} = \omega_{1p} t_1, \quad \xi_{\text{forbidden}} = \omega_{1p,f} t_1 \tag{9}$$

To excite the line, this angle should be $\xi \approx \pi/2$. Supposing that B_1 of the preparation pulse equals 10 μT, then for the allowed ESR transitions, strong lines are already expected for the duration of the preparation pulse of about $t_{1,\text{allowed}} = 1$ μs. However, to get pronounced lines for the forbidden transitions, one needs to use pulses with a much longer duration. In the case considered here, the shortest optimal pulse should be of the duration $t_{1,\text{forbidden}} = t_{1,\text{allowed}} \sqrt{2\omega_\alpha/|T_{zx}|}$, μs $\gg 1$ μs.

Another observation from this model concerns widths of the transitions. The forbidden transitions are extremely narrow compared to those of the allowed ones. In fact, this is an expected result. Indeed, the shape of the line is determined by the equation similar to eq 7

$$P_{\text{holeshape}} = \left(\frac{\omega_{1p}^2}{\Delta^2 + \omega_{1p}^2} \right) \sin^2 \left(\frac{(\Delta^2 + \omega_{1p}^2)^{1/2} t_1}{2} \right), \text{ where } \Delta = w^{(1)} - w_{nk} \tag{10}$$

According to this result, the width of the transition amounts to $2\omega_{1p}$. Therefore, the line width of the forbidden transition should be much narrower than that of the allowed transition. In the situation $(\Delta^2 + \omega_{1p}^2)^{1/2} t_1 \gg 1$, the line shape will be given by the Lorenzian function.[13] The simulated spectra in Figure 3 confirm this expectation.

In real systems, there might be an inhomogeneous broadening of the ESR transition frequencies, e.g., due to slightly different orientations of the molecules in a crystal matrix (distribution of angles θ in eq 2) and/or an unresolved super-hyperfine interaction with magnetic nuclei of the matrix. These mechanisms should contribute to the broadening of all lines in the EDNMR spectrum equally. However, in any case, the total width of the lines corresponding to the allowed transitions should be larger than that of lines arising from the forbidden transitions.

According to eq 3, the EDNMR spectrum has a mirror symmetry relative to its center. However, this symmetry can be broken due to the quadrupole interaction.

Figure 4 shows how the asymmetry in the EDMR spectrum arises by switching on the quadrupole interaction and increasing its strength D. It affects both the frequency position and intensities of lines in the EDNMR spectrum. Therefore, when the EDMR spectrum detected in an experiment appears symmetric, it seems to be safe to ignore an effect of the nuclear
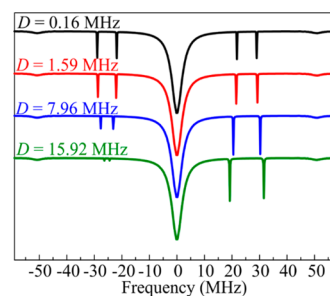

Figure 4. Manifestation of the nuclear spin quadrupole interaction in a shape of the EDNMR spectrum for different values of D. $B_{1p} = 0.8$ G and $t_1 = 6$ μs were used for the simulation. All other parameters are the same as those used for the simulations in Figure 3.

spin quadrupole interaction when analyzing experimental data. This result of the model can be instructive when studying real systems (see below). Note, the asymmetry due to quadruple interactions is observed, for example, in ref 10.

3. EXPERIMENTAL DETAILS

The formation of **1@3** and **2@3**, as well as the solid state structures of complexes **1−4**, determined by single-crystal X-ray diffraction studies are described in ref 16. The EDNMR experiments were performed on single crystals of **1@3** and **2@4** (Figure 6) with a Q-band ESR spectrometer Elexsys E580
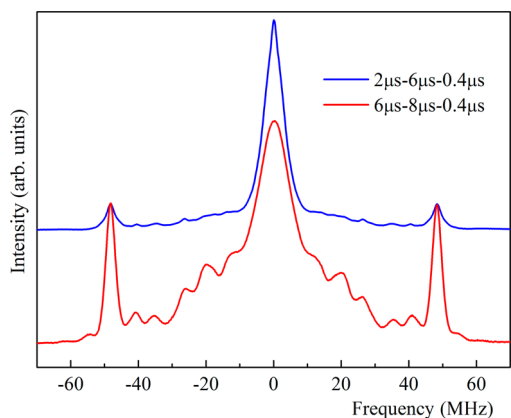

Figure 5. Comparison of the EDNMR spectra of **2@4** at the Q-band frequency at $T = 20$ K with different experimental settings. The upper spectrum was recorded with the ELDOR preparation pulse length of 2 μs, probe pulse length of 0.4 μs, and delay time of 6 μs, whereas the lower spectrum was recorded using respective pulse lengths of 6 and 0.4 μs and delay time of 8 μs.

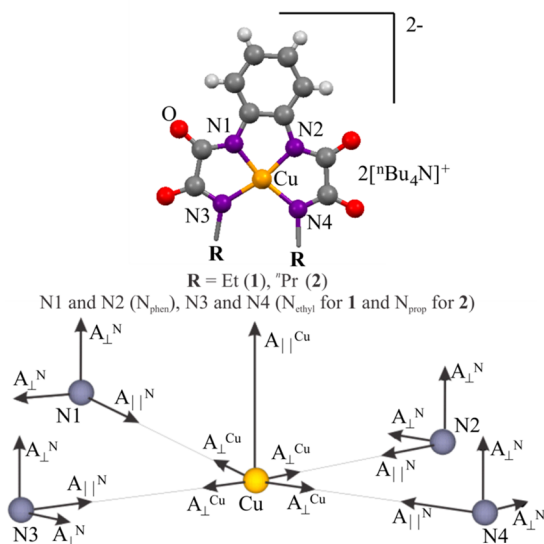**Figure 6.** (Top) Structure of the studied complexes with R = Et (**1**) and ^{n}Pr (**2**). (Bottom) Scheme of the principal axis of the Cu and N HF tensors.[16]

(Bruker) at a temperature of 20 K. The spectrometer was equipped with a standard cavity EN5107D2 inserted in the CF935 continuous flow cryostat. The temperature was controlled by the ITC 503 temperature controller. The bandwidth of the cavity at the overcouple mode amounted to

~100 MHz. The dual mw channels available in the spectrometer enabled dual mw frequency experiments. At first, the EDNMR spectra were measured at different mw frequencies. It was done to adjust the detection frequency to the maximum depth of the bandwidth profile of the resonator. In this situation, an EDNMR spectrum could be obtained in which the symmetric peaks relative to zero frequency (or detection frequency) have the same intensity. After that, the pump and detection pulse lengths were optimized to obtain the most resolved spectra (in terms of resolution and signal/noise ratio), as well as the pulse amplitudes (see Figure 5).

A first ELDOR preparation pulse ($\omega^{(1)}_{mw}$) with a length of 6 μs is the high turning angle pulse. The probe pulse ($\omega^{(2)}_{mw}$) is the $\pi/2$ pulse with a length of 0.4 μs creates an FID to record the EDESR spectrum. The probe pulse is applied after a delay time (τ) of 8 and 6 μs for **1@3** and **2@4**, respectively. The amplitude of the probe pulse amounted to ~7 MHz, and the pump pulse amplitude amounted to ~3 MHz (in the situation when the pump and observed frequencies are equal). For the detection of the EDNMR spectra, we have tried both the FID (one pulse) and the primary echo (two pulses) detection sequences. It turns out that in our particular experiment the FID detection provides better quality of the EDNMR spectra. Therefore, all EDNMR spectra were measured with the FID detection protocol. During the experiment, the integrated FID was recorded as a function of the mw frequency of the first pulse. The integration window was 1600 ns after the last pulse.

4. EDNMR EXPERIMENTS

A representative echo detected ESR spectrum of **1@3** at $T = 20$ K and for the direction of the magnetic field parallel to the normal of the molecular plane (0° orientation) is shown in Figure 7. All EDNMR measurements were carried out at a
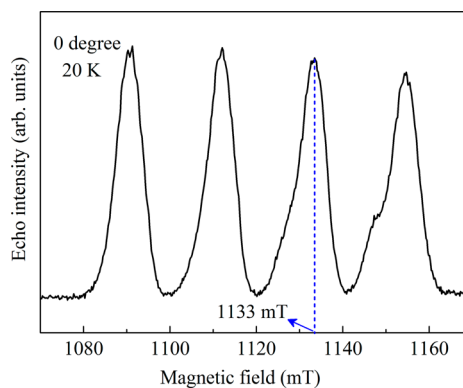

Figure 7. Experimental echo detected ESR spectrum of **1@3** at the Q-band frequency at $T = 20$ K for the magnetic field **B** applied parallel to the normal of the molecular plane (0° orientation).

magnitude of the magnetic field corresponding to the position of the third from the left line in the group of lines in the echo detected ESR spectra (~1130 mT). The EDNMR spectra of single crystals of **1@3** and **2@4** at 20 K at different orientations of the single crystals were recorded while the single crystals were rotated in the external magnetic field B_0 from 0° to 90° (field in the molecular plane). The results are shown in Figures 8 and 9. Well-resolved lines are observed in all orientations with a substantially better S/N ratio as compared to the pulsed ENDOR spectra of **1@3**.[16] This improvement can be explained by the different relaxation paths involved in the two
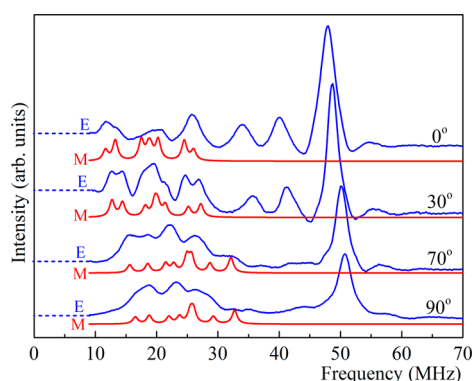
Figure 8. Experimental (E) and modeled (M) EDNMR spectra of **1@3** at the Q-band frequency at $T = 20$ K and at four orientations of the crystal in the external magnetic field B_0. 0° and 90° correspond to $B_0 \parallel$ and $B_0 \perp$ normal of the molecular plane. The central line at zero frequency has been subtracted from the experimental spectra. The first ELDOR preparation pulse length of 6 μs, probe pulse length of 0.4 μs, and delay time of 8 μs were set in the acquisition. Note that because the spectra were modeled with the ENDOR routine, the lines at frequencies above 35 MHz visible in the full EDNMR simulation (Figure 11) are not reproduced (see section 5).
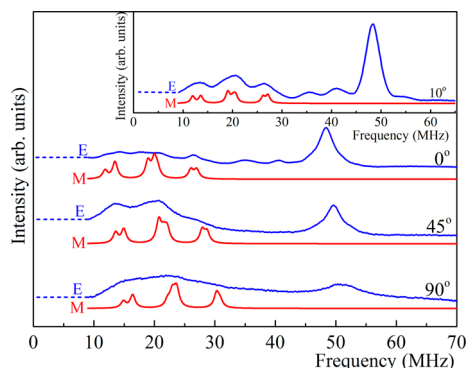
Figure 9. Experimental (E) and modeled (M) EDNMR spectra of **2@4** at the Q-band frequency at $T = 20$ K and at three orientations of the crystal in the external magnetic field B_0. 0° and 90° correspond to $B_0 \parallel$ and $B_0 \perp$ normal of the molecular plane. The first ELDOR preparation pulse length of 6 μs, probe pulse length of 0.4 μs, and delay time of 8 μs were set in the acquisition of the spectra. In the inset, the respective pulse lengths of 6 and 0.8 μs and delay time of 8 μs were set in the acquisition of the 10° spectrum. The central line at zero frequency has been subtracted from the experimental spectra. Note that because the spectra were modeled with the ENDOR routine, the lines at frequencies above 35 MHz visible in the full EDNMR simulation (Figure 11) are not reproduced (see section 5).

experiments and the smaller number of pulses in the EDNMR protocol.

For a correct assignment of the lines in the EDNMR spectrum, it is instructive to model the spectrum using our theoretical approach discussed in section 2. However, the simulation should be generalized to the case of four ^{14}N spins $I = 1$. It should be noted that the arithmetical sum of four spectra of the system with one $S = 1/2$ and one $I = 1$ with different HF constants might be insufficient to reproduce the complete spectrum, as additional lines in the more complex case of four ^{14}N spins coupled to the Cu electron spin are expected. This is illustrated in Figure 10, where results of a model calculation of the EDNMR spectra with increasing number of the coupled $I = $
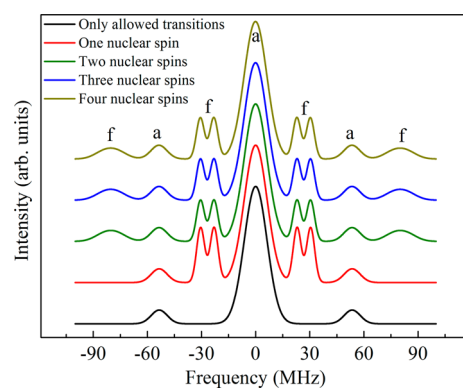

Figure 10. Model EDNMR spectra with the number n of nuclear spins $I = 1$ increasing from $n = 1$ to $n = 4$. Allowed and forbidden transitions are labeled as (a) and (f), respectively. Additional transitions appear if $n > 1$. The bottom spectrum is plotted to show the allowed transitions.

1 nuclei are shown. If more than one nuclear spin is coupled to the electron spins, additional lines arise in the spectrum.

In Figure 11, we show a simulated EDNMR spectrum for the case of one $S = 1/2$ and four $I = 1$ together with a
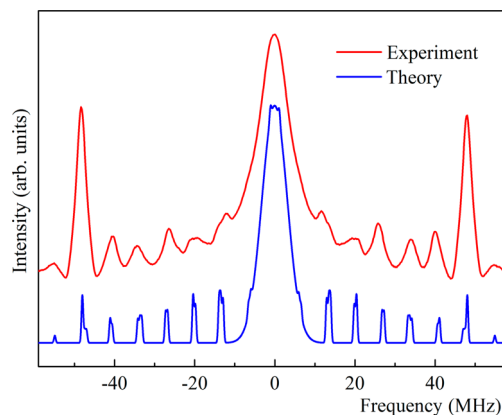

Figure 11. Comparison of the simulated and experimental EDNMR spectra of **1@3** for the case of one electron spin $S = 1/2$ of Cu(II) coupled to the ^{14}N nuclear spins I (^{14}N) = 1 of four nitrogen ligands. Simulation was performed assuming two nitrogen ligands with the HF constants $A_\perp^N(1) = 45$ MHz and $A_\parallel^N = 62$ MHz and the other two ligands with $A_\perp^N(1) = 33$ MHz and $A_\parallel^N = 48$ MHz.

representative experimental spectrum of **1@3**. All experimental lines are reasonably well reproduced in the simulation and therefore can be robustly assigned to the system of one electron spin $S = 1/2$ of Cu(II) coupled to the ^{14}N nuclear spins I (^{14}N) = 1 of four nitrogen ligands in the studied complexes. At the Q-band frequency, which corresponds to a magnetic field of ~1 T, the nitrogen (^{14}N) Larmor frequency is ~4 MHz, and the proton (^{1}H) Larmor frequency is ~50 MHz. Therefore, protons probably also contribute to the line in the EDNMR spectra at ~50 MHz (Figures 8, 9, and 11) . This would be consistent with our previous X-band ENDOR study.[16] There, a group of lines due to protons was spread in a range of ~5 MHz around their X-band Larmor frequency of ~14 MHz. In the Q-band, they all should then be correspondingly located within the broad line at ~50 MHz.

5. DISCUSSION

Analysis of the EDNMR Spectra. The theoretical treatment of EDNMR in the $S = 1/2$, $I = 1$ electron–nuclear system introduced in section 2 has highlighted that the quadruple interaction can manifest itself in a rather peculiar pattern of the EDNMR spectrum: the spectrum should become asymmetric not only with respect to the positions of the lines but also of the intensities of the lines if the quadrupole interaction is strong enough (see Figure 4). The experimental EDNMR spectra appear symmetric (Figures 8, 9, and 11). This observation enables the conclusion that, in the Cu complexes studied in our work, the nuclear spin quadrupole interaction should be small and can thus be neglected when analyzing the experimental data.

Because simulations of the full EDNMR spectra for the case of one electron spin $S = 1/2$ coupled to four nuclear spins $I = 1$ are cumbersome, and considering the fact that for the determination of the ^{14}N HF constants we are mainly interested in the positions of the forbidden transitions, we have used for the modeling a much faster ENDOR routine of the EasySpin software package. Specifically, to obtain the individual HF tensor of all four N donor atoms, we have modeled experimental spectra using an EasySpin (version 4.5.5)[22] program of the Matlab 2009b package. It does not contain a specific program to simulate the EDNMR spectra. However, the EDNMR spectra have the same transition frequencies as the ones found in an ENDOR experiment. Hence, the EDNMR spectra were modeled using the subprogram of EasySpin that simulates the ENDOR spectrum.

For the modeling with the EasySpin software package, we adopted the following spin Hamiltonian, which is similar to eq 1:

$$\mathcal{H} = \mu_B \vec{B}_0 \mathbf{g} \vec{S} + \vec{S} \mathbf{A}^{Cu} \vec{I}^{Cu} + \sum_{i=1}^{4} \vec{S} \mathbf{A}^{N} \vec{I}^{N_i} + \mu_n \vec{B}_0$$
$$\left(\sum_{i=1}^{4} g_n^{N_i} \vec{I}^{N_i} + g_n^{Cu} \vec{I}^{Cu} \right) \tag{11}$$

Here, the first term represents the Zeeman interaction of an electron spin S with the external magnetic field $\vec{B}_0$. g and μ_B stand for the g-tensor and Bohr magneton, respectively. The HF interaction between the electron spin S of Cu(II) and the nuclear spins of ^{63}Cu, ^{65}Cu, and ^{14}N are described by the second and third terms, respectively. A^{Cu} and A^{N} are the respective HF coupling tensors. The last term presents the nuclear Zeeman interaction of the nuclear spins of four N and the nuclear spin of Cu with the external magnetic field $\vec{B}_0$.

To simulate the spectra, we considered the HF interaction between the ^{14}N nuclear spins I (^{14}N) = 1 of four nitrogen ligands and the unpaired electron at the central Cu(II) metal ion (scheme in Figure 6) under the following assumption

$$g_X = g_Y = g_\perp, \; g_Z = g_\parallel, \; A_X = A_Y = A_\perp < A_Z = A_\parallel \tag{12}$$

We have taken the values of the g-factor and the on-site HF coupling tensors for Cu(II) from our previous work.[16]

The results of the modeling are shown in Figures 8 and 9 together with experimental spectra. They agree well with each other, confirming that indeed the EDNMR enables us to resolve all four nitrogen HF tensors. Note that because the ENDOR routine models only NMR transitions that correspond to the forbidden transition in the EDNMR spectrum, the lines above 35 MHz reproduced in the full EDNMR simulation

(Figure 11) are not present here. A finite intensity of the forbidden transitions in the experimental spectra at symmetric orientations of 0° and 90° indicates some misorientation of the crystals. However, because the position of the lines near these orientations has a small angular dependence, this does not affect the estimates of the HF tensors. Principal values of A^{N} for **1** and **2** obtained from the simulation are listed in Table 1.

Table 1. Principal Values of the HF tensor A^{N} (MHz) of 1 and 2

compound	$A_\perp^{N}$	$A_\parallel^{N}$	A_{iso}
1	Group A: N1:45, N2:33	Group A: N1:62, N2:48	Group A: N1:51, N2:46
	Group B: N3:42, N4:30	Group B: N3:54, N4:42	Group B: N3:38, N4:34
2	Group A: N1:46, N2:44	Group A: N1:58, N2:56	Group A: N1:50, N2:48
	Group B: N3:34, N4:31	Group B: N3:42, N4:40	Group B: N3:37, N4:34

When the magnetic field is perpendicular to the molecular plane, the largest ^{14}N HF constants are obtained consistently with our previous ESR and ENDOR measurements found in ref 16. The HF tensors reported in Table 1 indicate two different groups of N ligands, classified as groups A and B. The ^{14}N HF constants for group A are close to those in the related Cu(II)–(bis)oxamidato complex containing only two phenylene-bridged nitrogen ligands.[23] Therefore, group A can be assigned to the nitrogen ligands bridged with phenylene (N_{phen}). Group B, with smaller ^{14}N HF constants, can be assigned to nitrogens bridged with ethyl (N_{ethyl}) and nitrogens bridged with propyl (N_{prop}) for **1** and **2**, respectively.

The obtained ^{14}N HF tensors for **1** are in a general qualitative agreement with our previous results of the ENDOR measurements on the same complex[16] and enable us to reproduce the experimental ENDOR spectrum well. However, in detail, there are certain quantitative differences of the order of ~10%. Taking into account a better quality of the present EDNMR spectra, the values of the ^{14}N HF constants in Table 1 are obviously more accurate. Thus, it is appealing to revisit the estimates of the electron spin densities on the nitrogen ligands in **1** and also to perform respective calculations for complex **2** using the HF tensor determined for the first time in the present work.

Estimates of the Electron Spin Densities on N Ligands. The transferred HF coupling arises due to an overlap of the orbitals of the central metal ion and of the ligands. Therefore, the HF constants are expected to correlate with a transfer of the electron spin density from the paramagnetic ion to the neighbor atoms. To estimate the spin density on the N-donor atoms from experimentally obtained ^{14}N HF coupling constants for **1** and **2**, we have used the model introduced by Morton and Preston.[17] According to this approach, the spin densities ρ^s and ρ^p on the s and p orbitals are proportional to the isotropic or Fermi contact contribution A_{iso} and the dipolar HF coupling constant $A_{dip} = A_{iso} - A_\perp$, respectively. A more detailed description of this model can be found in our previous work.[24] One can obtain the isotropic ^{14}N HF constant for each N atom from the ^{14}N HF tensor components with the equation

$$A_{iso} = 1/3(2A_\perp + A_\parallel) \tag{13}$$

The results for complexes **1** and **2** are listed in Table 1. Following the standard calculus as described in ref 24, the spin

Table 2. Spin Density (in %) on N Donor Atoms in 1 and 2

compound	N1			N2			N3			N4		
	ρ^S	ρ^P	ρ^{total}	ρ^S	ρ^P	ρ^{total}	ρ^S	ρ^P	ρ^{total}	ρ^S	ρ^P	ρ^{total}
1	2.82	10.21	13	2.10	9.00	11.10	2.54	7.20	9.74	1.88	7.20	9.08
2	2.76	7.20	9.96	2.65	7.20	9.85	2.04	4.80	6.84	1.88	5.40	7.28

densities ρ on the s (ρ^s) and p (ρ^p) orbitals of the N-donor atoms together with the total spin densities ρ^{total} on the N-donor atoms for **1** and **2** have been estimated. The results are summarized in Table 2.

As expected, the major partial spin density resides on the p orbitals. Furthermore, the spin density on the individual N donor atoms reveals an unequal distribution. The spin density on N_{ethyl} and N_{prop} atoms for **1** and **2**, respectively, is smaller than that on N_{phen} atoms of the respective complexes. Importantly, due to a better quality of the present EDNMR data, we can now resolve the controversy of the previous ENDOR based estimate made for **1**, where the spin density on one of the N_{ethyl} donor atoms turns out to be 1.5× larger than for the second one (Table 8 in ref 16). This is not confirmed in the current analysis, where similar values for both N_{ethyl} donor atoms have been obtained. Most likely, that earlier contradiction was caused by limited accuracy of the ENDOR experiment, which has led to an overestimate of the anisotropy $(A_\parallel - A_\perp)$ and thus to an overestimate of ρ^p for one of the N_{ethyl} donor atoms.

The estimates of ρ from the HF tensors of **1** and **2** appear systematically smaller than the predictions of the DFT calculations in ref 16. This deviation is not surprising considering simplifications of the model by Morton and Preston.[17] Specifically, deviations from a square planar molecular geometry assumed in the model could be responsible for this discrepancy. However, it is important to emphasize a qualitative agreement with the DFT results, in particular that the EDNMR-based estimates confirm the DFT prediction on the unequal distribution of the spin densities between the N_{phen} donor atoms on one side and the N_{ethyl} or N_{prop} donor atoms on the other.

In a recent study, we pointed out a correlation between the spin density distribution in heteroatom-substituted mononuclear bis(oxamidato)-type Cu(II) complexes and the magnetic exchange coupling in the corresponding trinuclear complexes.[24] Considering this, we can conjecture that the observed smaller spin density on the N_{ethyl} atoms of **1** and N_{prop} atoms of **2** compared to the spin density on the N_{phen} atoms in **1** and **2** could be an indication of weaker magnetic exchange interaction along the paths Cu-N_{ethyl}-O-Cu and Cu-N_{prop}-O-Cu for **6** and **7**, respectively, compared to that along Cu-N_{phen}-O-Cu (Figure 12).

One should bear in mind however that a transfer of the spin density to the ligand is just one of the factors that facilitates magnetic exchange between the metal centers, nor less important is the real geometry of the bondings involved, which could be finally decisive for the interaction strength J. From a comparison between the spin densities on the N donor atoms of **1** and **2**, which is somewhat smaller for the latter complex (Table 2), the J value for corresponding trinuclear complex **7** can be expected to be lower than that for **6**. However, the larger J value for **7** ($J = -132$ cm^{-1}) relative to that of **6** ($J = -104$ cm^{-1}) has been deduced from the temperature dependence of the magnetic susceptibility.[16] This counterintuitive result can be explained by considering the local
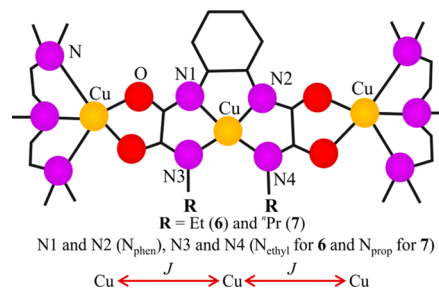

Figure 12. Structure of the trinuclear Cu(II) complexes with **R** = Et (**6**) and ^{n}Pr (**7**). The magnetic exchange J between the Cu spins takes place via exchange paths Cu–N_{phen}–O-Cu, and Cu–N_{ethyl}–O-Cu (**6**) and Cu–N_{prop}–O-Cu (**7**), respectively.

geometry of the terminal Cu(II) ions (Figure 10). In addition to the coordination geometry of the central Cu(II) ion for trinuclear complexes, the strength of the magnetic super-exchange interactions between neighboring Cu(II) spins can be influenced by the coordination geometry of the terminal Cu(II) ions.[25] The terminal Cu(II) ions for **6** and **7** are coordinated in a distorted square pyramidal fashion. When the distortion increases, the contribution of the d_{z^2} orbitals of the terminal Cu(II) ions to the magnetic pathway increases. These orbitals are directed in the plane of the central Cu(II) orbital, which results in a larger overlap between the magnetic orbitals. Subsequently, the magnitude of the superexchange interactions between neighboring Cu(II) spins is enhanced. Therefore, the observed larger J value for **7** can be due to the increased distortion of the square pyramidal geometry of the terminal Cu(II) ions of **7** in comparison to **6**. A similar effect has been observed previously in the related trinuclear bis(oxamato) complexes found in ref 25. This can explain an apparent controversy that despite a larger spin density on N donor atoms for **1** the J value for its corresponding trinuclear complex **6** appears smaller than that for **7**.

6. CONCLUSIONS

We have experimentally investigated diamagnetically diluted single crystalline mononuclear complexes of [$^nBu_4N$]$_2$[Cu-(opboR$_2$)] (R = C$_2$H$_5$ **1**, C$_3$H$_7$ **2**) (1%) in a host lattice of [$^nBu_4N$]$_2$[Ni(opboR$_2$)] (R = C$_2$H$_5$ **3**, C$_3$H$_7$ **4**) (99%) (**1@3** and **2@4**) with the EDNMR technique. It appears that the EDNMR spectrum of the system studied is symmetric, implying negligible nuclear quadrupole interaction. Importantly, in our theoretical model for the EDNMR spectrum of the electron–nuclear coupled system with $S = 1/2$ and $I = 1$ treated with the spin density matrix approach, we find that a strong nuclear quadrupole interaction should cause substantial asymmetry of the EDNMR spectrum, not only with regard to the frequency shifts of the forbidden transitions, but also of the asymmetry of their intensities. The analysis of the EDNMR spectra facilitated by this theoretical treatment has enabled an accurate determination of the hyperfine tensors of all four nitrogen ligands of the central metal ion beyond the limitations of previously applied cw ESR and ENDOR methods.[16] The

analysis of the HF tensors enables an estimation of the leakage of the spin density from Cu(II) toward nitrogens. The spin density appears to be larger on N_{ethyl} and N_{prop} atoms for **1** and **2**, respectively, as compared to N_{phen} atoms, in qualitative agreement with the earlier DFT calculations.[16] Because a transfer of the spin density to the bonding ligand is a prerequisite for a magnetic exchange coupling between paramagnetic atoms, the revealed disproportionality of the spin densities implies that, in the respective trimetallic complexes $[Cu_3(opboR_2) (pmdta)_2](NO_3)_2$ (R = Et **6**, ^nPr **7**), the Cu-N_{phen}-O-Cu exchange path is stronger than the Cu-N_{ethyl}-O-Cu and Cu-N_{prop}-O-Cu ones for **6** and **7**, respectively. Finally, we point out that the larger exchange constant J observed for **7** as compared to **6**, despite the somewhat smaller spin density on the N donor atoms in the respective monometallic complex **2** as compared to that of **1**, can be ascribed to a more favorable magnetic exchange coordination geometry of the terminal Cu(II) atoms in **7**.

■ AUTHOR INFORMATION

Corresponding Author

*E-mail: V.Kataev@ifw-dresden.de.

Notes

The authors declare no competing financial interest.

■ ACKNOWLEDGMENTS

■ REFERENCES

(1) Mims, W. B. Envelope Modulation in Spin-Echo Experiments. *Phys. Rev. B* **1972**, *S*, 2409−2419.

(2) Bekauri, P. I.; Berulava, B. G.; Khakhana, Og; Sanadze, T. I. Discrete Saturation on EPR Lines. *Phys. Lett. A* **1967**, *A 24*, 156−158.

(3) Bekauri, P. I.; Berulava, B. G.; Sanadze, T. I.; Khakhana, Og. Discrete Saturation of Inhomogeneously Broadened EPR Lines. *Soviet Physics Jetp* **1967**, *25*, 292−296.

(4) Sanadze, T. I.; Khutsish, Gr. Forbidden Transitions and Discrete Saturation in EPR Lines. *Soviet Physics Jetp* **1969**, *29*, 248−251.

(5) Wacker, T.; Schweiger, A. Fourier-Transform EPR-Detected NMR. *Chem. Phys. Lett.* **1991**, *186*, 27−34.

(6) Davies, E. R. New Pulse ENDOR Technique. *Phys. Lett. A* **1974**, *A 47*, 1−2.

(7) Mims, W. B. Pulsed ENDOR Experiments. *Proc. R. Soc. London, Ser. A* **1965**, *283*, 452−457.

(8) Schosseler, P.; Wacker, T.; Schweiger, A. Pulsed ELDOR Detected NMR. *Chem. Phys. Lett.* **1994**, *224*, 319−324.

(9) Potapov, A.; Epel, B.; Goldfarb, D. A Triple Resonance Hyperfine Sublevel Correlation Experiment for Assignment of Electron-Nuclear Double Resonance Lines. *J. Chem. Phys.* **2008**, *128*, 052320.

(10) Florent, M.; Kaminker, I.; Nagarajan, V.; Goldfarb, D. Determination of the N-14 Quadrupole Coupling Constant of Nitroxide Spin Probes by W-band ELDOR-detected NMR. *J. Magn. Reson.* **2011**, *210*, 192−199.

(11) Van Doorslaer, S.; Vinck, E. The Strength of EPR and ENDOR Techniques in Revealing Structure-Function Relationships in Metalloproteins. *Phys. Chem. Chem. Phys.* **2007**, *9*, 4620−4638.

(12) Kaminker, I.; Wilson, T. D.; Savelieff, M. G.; Hovav, Y.; Zimmermann, H.; Lu, Y.; Goldfarb, D. Correlating Nuclear Frequencies by Two-Dimensional ELDOR-detected NMR Spectroscopy. *J. Magn. Reson.* **2014**, *240*, 77−89.

(13) Nalepa, A.; Mobius, K.; Lubitz, W.; Savitsky, A. High-field ELDOR-detected NMR Study of a Nitroxide Radical in Disordered Solids: Towards Characterization of Heterogeneity of Microenvironments in Spin-labeled Systems. *J. Magn. Reson.* **2014**, *242*, 203−213.

(14) Bruch, E. M.; Warner, M. T.; Thomine, S.; Tabares, L. C.; Un, S. Pulse Electron Double Resonance Detected Multinuclear NMR Spectra of Distant and Low Sensitivity Nuclei and Its Application to the Structure of Mn(II) Centers in Organisms. *J. Phys. Chem. B* **2015**, 150311150806001.

(15) Abdulmalic, M. A.; Aliabadi, A.; Petr, A.; Krupskaya, Y.; Kataev, V.; Buchner, B.; Hahn, T.; Kortus, J.; Ruffer, T. An Interplay Between the Spin Density Distribution and Magnetic Superexchange Interactions: a Case Study of Mononuclear (Bu4N)-Bu-n (2) Cu(opooMe) and Novel Asymmetric Trinuclear Cu-3(opooMe) (pmdta)(2) (NO3)(2)center dot 3MeCN. *Dalton Trans.* **2012**, *41*, 14657−14670.

(16) Abdulmalic, M. A.; Aliabadi, A.; Petr, A.; Krupskaya, Y.; Kataev, V.; Büchner, B.; Zaripov, R.; Vavilova, E.; Voronkova, V.; Salikov, K.; et al. Magnetic Superexchange Interactions: Trinuclear bis(oxamidato) Versus bis(oxamato) Type Complexes. *Dalton Trans.* **2015**, *44*, 8062.

(17) Morton, J. R.; Preston, K. F. Atomic Parameters for Paramagnetic-Resonance Data. *J. Magn. Reson.* **1978**, *30*, 577−582.

(18) Maki, A. H.; McGarvey, B. R. Electron Spin Resonance in Transition Metal Chelates 0.1. Copper(Ii) Bis-Acetylacetonate. *J. Chem. Phys.* **1958**, *29*, 31−34.

(19) Dikanov, S. A.; Tsvetkov, Y. *Electron Spin Echo Envelope Modulation (ESEEM) Spectroscopy*; CRC Press: Boca Raton, FL, 1992.

(20) Ernst, R. R.; Bodenhausen, G.; Wokaun, A. *Principles of Nuclear Magnetic Resonance in One and Two Dimensions*; Oxford University Press: Oxford, 1987.

(21) Abragam, A. *The Principles of Nuclear Magnetism*; Oxford University Press: Oxford, 1961.

(22) Stoll, S.; Schweiger, A. EasySpin, a Comprehensive Software Package for Spectral Simulation and Analysis in EPR. *J. Magn. Reson.* **2006**, *178*, 42−55.

(23) Brauer, B.; Weigend, F.; Fittipaldi, M.; Gatteschi, D.; Reijerse, E. J.; Guerri, A.; Ciattini, S.; Salvan, G.; Ruffer, T. Electron Paramagnetic Resonance and Density-Functional Theory Studies of Cu(II)-bis-(oxamato) Complexes. *Inorg. Chem.* **2008**, *47*, 6633−6644.

(24) Abdulmalic, M. A.; Aliabadi, A.; Petr, A.; Krupskaya, Y.; Kataev, V.; Buchner, B.; Hahn, T.; Kortus, J.; Ruffer, T. An Interplay Between the Spin Density Distribution and Magnetic Superexchange Interactions: a Case Study of Mononuclear (Bu4N)-Bu-n (2) Cu(opooMe) and Novel Asymmetric Trinuclear Cu-3(opooMe) (pmdta)(2) (NO3)(2)center dot 3MeCN. *Dalton Trans.* **2012**, *41*, 14657−14670.

(25) Costa, R.; Garcia, A.; Ribas, J.; Mallah, T.; Journaux, Y.; Sletten, J.; Solans, X.; Rodriguez, V. Tailored Magnetic-Properties in Trinuclear Copper(Ii) Complexes - Synthesis, Structure, and Magnetic-Properties of Complexes Derived from 1,3-Propanediylbis-(Oxamato) Cuprate(Ii) (Cu(Pba) 2-). *Inorg. Chem.* **1993**, *32*, 3733−3742.